Article

High-Density Cobalt Single-Atom Catalysts for Enhanced Oxygen Evolution Reaction

Pawan Kumar,* Karthick Kannimuthu,○ Ali Shayesteh Zeraati,○ Soumyabrata Roy, Xiao Wang, Xiyang Wang, Subhajyoti Samanta, Kristen A. Miller, Maria Molina, Dhwanil Trivedi, Jehad Abed, M. Astrid Campos Mata, Hasan Al-Mahayni, Jonas Baltrusaitis, George Shimizu, Yimin A. Wu, Ali Seifitokaldani, Edward H. Sargent, Pulickel M. Ajayan, Jinguang Hu,* and Md Golam Kibria*
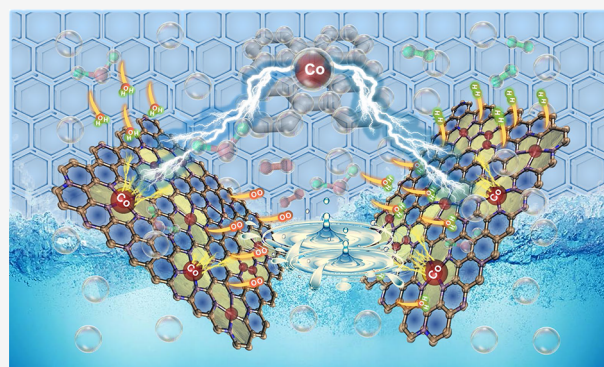
Read Online

ACCESS | Metrics & More | Article Recommendations | Supporting Information

ABSTRACT: Single atom catalysts (SACs) possess unique catalytic properties due to low-coordination and unsaturated active sites. However, the demonstrated performance of SACs is limited by low SAC loading, poor metal−support interactions, and nonstable performance. Herein, we report a macromolecule-assisted SAC synthesis approach that enabled us to demonstrate high-density Co single atoms (10.6 wt % Co SAC) in a pyridinic N-rich graphenic network. The highly porous carbon network (surface area of ∼186 m^2 g^{-1}) with increased conjugation and vicinal Co site decoration in Co SACs significantly enhanced the electrocatalytic oxygen evolution reaction (OER) in 1 M KOH (η_{10} at 351 mV; mass activity of 2209 mA mg$_{Co}^{-1}$ at 1.65 V) with more than 300 h stability. Operando X-ray absorption near-edge structure demonstrates the formation of electron-deficient Co-O coordination intermediates, accelerating OER kinetics. Density functional theory (DFT) calculations reveal the facile electron transfer from cobalt to oxygen species-accelerated OER.

INTRODUCTION

The dwindling price of renewable energy systems has garnered interest in electrochemical technologies such as fuel cells, rechargeable metal-air batteries, water electrolysis, and CO$_2$ conversion technologies.[1,2] Electrocatalytic water splitting offers a modular approach to producing hydrogen; however, anodic oxygen evolution reaction (OER) impedes performance by consuming 90% of the energy input.[3] Recently, noble metals (Ir, Ru, etc.)-based single-atom catalysts (SACs) integrated with 3d transition metal oxide-based networks have shown promising performance in OER.[4,5] However, further improvements are required in near future for industrial-scale performance. Transition metal-based SACs with M−N$_x$−C moieties embedded in nitrogen (N)-doped carbonaceous scaffolds are emerging as an alternative to noble metal catalysts for thermo-/ and electrocatalysis.[6−8] The presence of isolated undercoordinated metal centers stabilized via N-coordination, and discretized energy levels ensure high activity, stability, and metal economy. However, high-temperature synthesis of M−N$_x$−C SACs using C−N precursors and metal salts rarely reaches isolated atom density above unity (∼1.0−1.5%). Further increase in metal content leads to agglomeration, limiting the performance below the benchmark (Pt/C, Ir/C) catalysts.[9,10] The single-atom sites pinned in the defect-rich graphene lattice have also been widely investigated. However, the unsymmetric C and N terminated vacancies limit the metal concentration, while the low N content promotes agglomeration, reducing the efficacy of isolated sites.[11,12] The fabrication of densely populated M−N$_x$−C SACs is essential for the colligative enhancement of catalytic performance, and close proximity of metal centers also enables "cooperative catalysis".[13]

Recently, Zhao et al. proposed a cascade anchoring strategy utilizing the complexation of metal and glucose followed by annealing with melamine to afford a maximum 12.1 wt % metal loading in a graphenic network. However, two-step annealing and the requirement of layer-by-layer deposition on oxygen-rich porous carbon supports impede the scalability.[14] The carbonization of metal−organic frameworks (MOFs) that are constituted of metal-containing nodes and organic linkers is

A
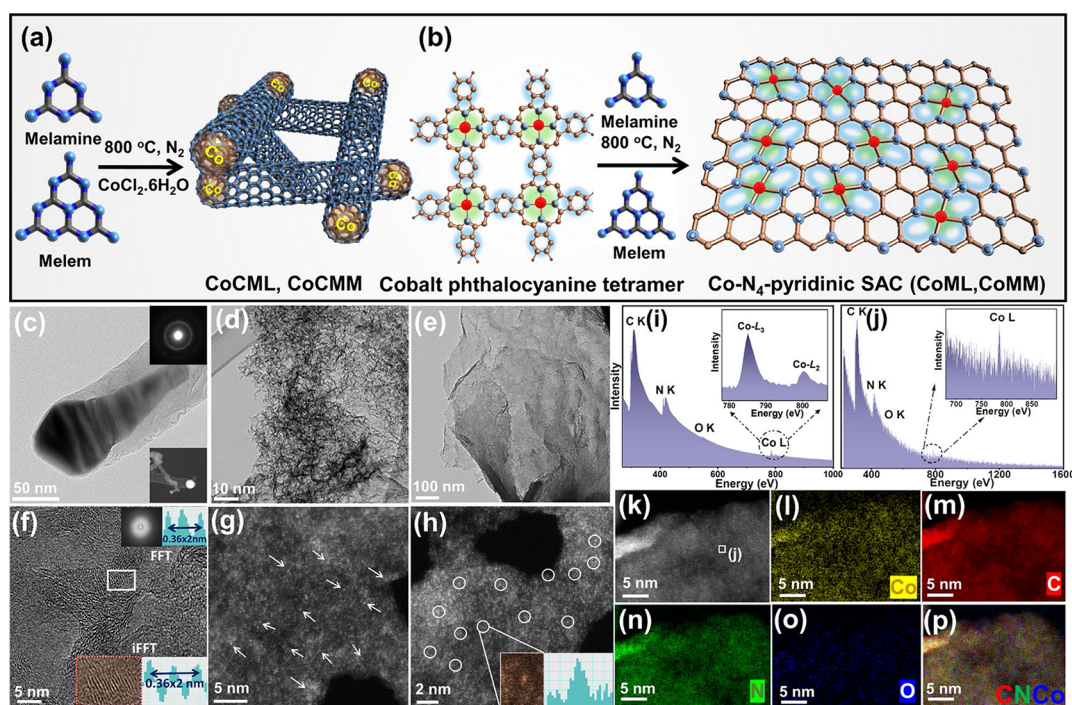
Figure 1. Schematic diagram of the synthesis of (a) nanocluster CoCML and CoCMM using thermal condensation (800 °C) of melamine and melem, respectively. (b) Co−N₄-pyridinic SACs using thermal condensation of cobalt phthalocyanine tetramer (CoPc) with melem (CoMM) and CoPc with melamine (CoML). (c) HR-TEM images of CoCMM showing Co entrapped carbonaceous nanotubular structure; inset showing FFT of the image. (d) HR-TEM image of CoMM showing the porous structure. (e) HR-TEM image of CoML. (f) HR-TEM of CoMM showing lattice fringes and d-spacing. AC-HAADF STEM images of CoMM at (g) 5 nm and (h) 2 nm scale bar; white arrow and circles displaying bright spots as cobalt single atoms. Inset in (h) is showing the line scan showing Z-contrast. (i) EELS spectrum of CoMM from the complete area in image k. (j) EELS spectrum of a small square marked in the image k. (l−p) EELS mapping for Co, C, N, and O and RGB composite of C, N, and Co.

the most popular approach to fabricate high-density M−N$_x$−C SACs.[15] Wu et al. demonstrated the synthesis of high-density Co (≈15.3%) M−N$_x$−C catalysts using a Co-based zeolitic organic framework (ZIF-67) which exhibits an oxygen reduction reaction (ORR) performance of ≈12.164 A mg$_{Co}$$^{-1}$ at 0.8 V (10.5 times higher than Pt/C).[16] Despite higher metal loading, agglomeration and nanoparticle (NP) formation are often reported in this synthesis approach, which limit the availability of single atomic sites. Due to the low thermal stability of ligands, the metal centers tend to release prematurely, leading to high mobility and agglomeration.[17−19] Furthermore, the lack of functional groups for condensation with carbonaceous/nitrogenous frameworks also accelerates nanoparticle (NP) formation. Despite higher metal loading, the use of expensive organic ligands and acid etching to remove nanocluster/nanoparticulate limits their scalability. Recently, Xia et al. trapped various metals (Ir, Pt, Ni, etc.) in NH₂-functionalized graphene quantum dots (GQDs−NH₂). The subsequent thermal annealing of the freeze-dried mixture of M-GQDs-NH₂ and urea led to an exceptionally high single-atom (SA) loading (i.e., Ir-40 wt % or 3.8 at %) and N content (27.8 at %).[20] These observations suggest that the concurrent presence of metal coordination sites and functional groups is essential for the growth of the carbon framework to achieve high SA concentrations. Based on these observations, we hypothesize that metal ions trapped in a stable flat molecule with plenty of functional groups can provide numerous fusion sites to afford higher metal content M−N$_x$−C SACs.

Herein, we report on a synthesis approach that enables densely populated Co SAC (10.6 wt %, 3.18 at %) embedded in N-rich carbonaceous scaffold by condensation of cobalt phthalocyanine tetramers (CoPc) and melem moieties (CoMM). The planar CoPc and melem (C₆N₇) core fusion in CoMM allows N content to exceed ~52 at %, which is dominated by pyridinic nitrogen. The C−N matrix in CoMM reveals a ~1:1 C−N stoichiometry with periodic C and N arrangement, originating from the direct fusion of heptazine (C₆N₇) units. Such high N content with precise atomic arrangement is seldom reported in a graphenic network and only predicted using DFT models.[21,22] CoMM displayed a nanoporous structure with a high specific surface area (S$_{BET}$ 186 m² g^{-1}; C$_{dl}$ of 8.71 mF cm^{-2}). Under optimized conditions, CoMM exhibits enhanced OER (η_{10} at 351 mV; mass activity of 2209 mA mg$_{Co}$$^{-1}$ at 1.65 V) performance with >300 h stability. The high concentration of Co embedded in N-rich porous carbon frameworks and enhanced conjugation degrees synergistically facilitate better OER performance.

■ RESULTS AND DISCUSSION

Synthesis and Characterization of SA Co−N₄ (Pyridinic) and Metallic Co Nanoparticles Embedded in Carbonaceous Structures. To demonstrate the role of high-temperature thermal condensation in the commonly reported synthesis approach, we started the synthesis with two precursors, i.e., melamine and melem (see the Supporting Information for experimental details) (Figure 1a,b).[23,24] The material prepared using melamine was labeled as CoCML while using melem was referred to as CoCMM. SEM images and elemental mapping of CoCML and CoCMM displayed long carbon-rich nanotubes with metallic Co NPs entrapped at the tip (Figures S1−S2). The high-resolution transmission electron microscopy (HR-TEM) images of CoCMM exhibited
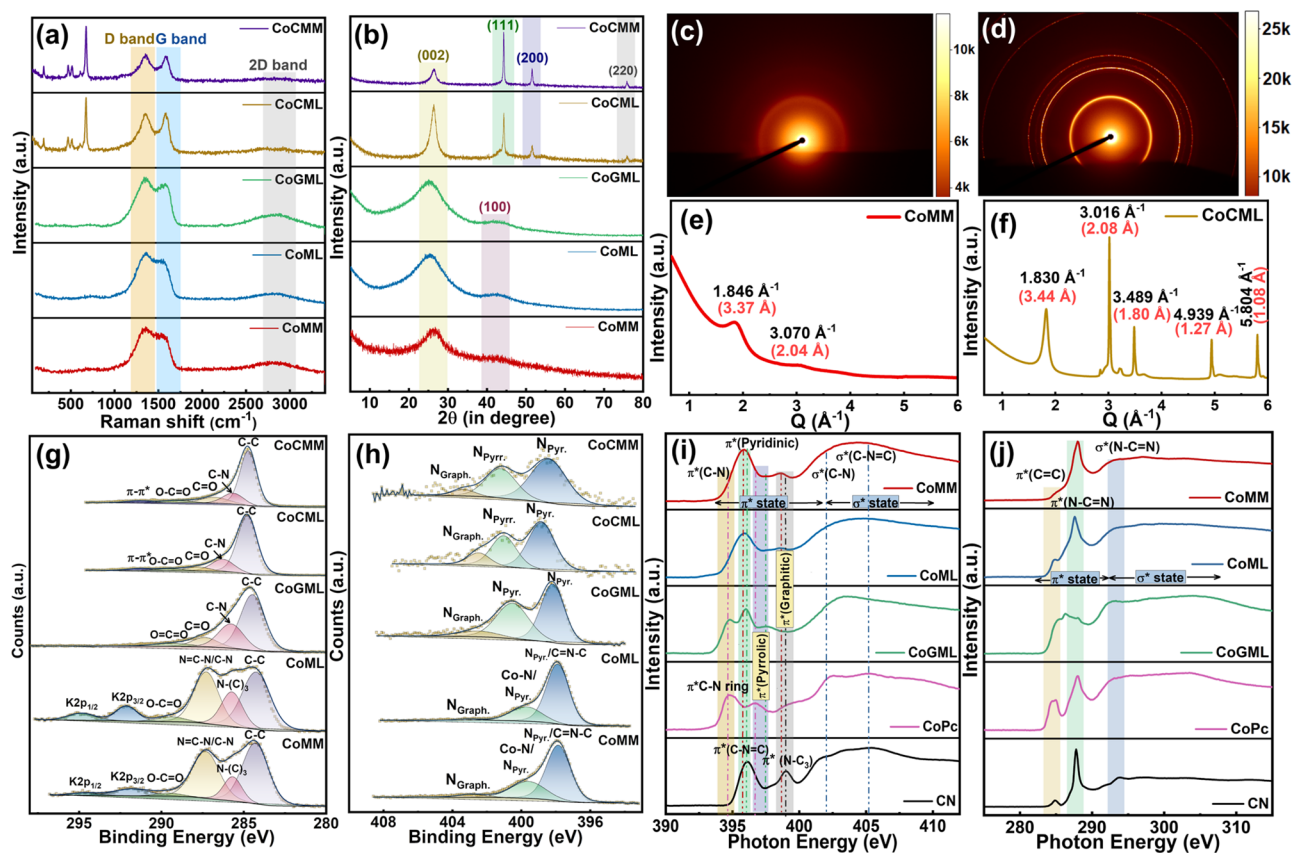
Figure 2. (a) Raman and (b) XRD pattern of CoMM, CoML, CoGML, CoCML, and CoCMM (Bottom to top). Synchrotron-based WAXS 2D images of (c) CoMM and (d) CoCML, calculated Q value of (e) CoMM and (f) CoCML. (g) C 1s and (h) N1s XPS spectra of CoMM, CoML, CoGML, CoCML, and CoCMM (Bottom to top). $N_{pyr.}$ stands for pyridinic Ns, while $N_{pyrr.}$ stands for pyrrolic Ns. (i) N K-edge and (j) C K-edge NEXAFS spectra of CN, CoPc, CoGML, CoML, and CoMM (Bottom to top).

dense metallic Co NPs encased in the crystalline graphitic network (Figures 1c and S3). Well-defined lattice fringes with 0.37 nm d-spacing for stacked carbon and 0.225 nm for metallic cobalt were observed along with two sharp diffraction rings, demonstrating Co-promoted graphitization in CoCMM. Similar nanostructural features were observed for the CoCML except less ordered carbon stacking, suggesting that planar melem promotes better graphitization in CoCMM (Figure S4). The degradation of nitrogenous precursors at high temperatures reduces unbound Co^{2+} species to metallic Co(0) which form nanoclusters due to high surface energy and serve as the catalyst for the graphitization of amorphous carbon.[25]

Interestingly, when the cobalt phthalocyanine hexadecacarboxylic acid tetramer (CoPc) (Scheme S1, Figure S6, and Table S1 in SI) was used as a preconfined source of Co, isolated Co−N₄ SA sites embedded in the C−N framework were achieved (Figure 1b). The Co−N₄ SACs prepared using CoPc and melamine were denoted as CoML while the sample prepared using CoPc and melem was referred to as CoMM. We also prepared a control sample using glucose, melamine, and CoPc denoted as CoGML (Figure S5). The CoMM synthesized using CoPc and melem demonstrates a highly porous structure (S_{BET}-186 m² g⁻¹) with well-distributed Co in the C−N matrix (Figures 1d and S7−8, Table S2). In contrast, CoML fabricated using CoPc and melamine exhibited a nonporous graphenic structure (S_{BET} of 37.81 m² g⁻¹), implying different condensation mechanisms in melem and melamine-derived SACs (Figures 1e and S9, Table S2). A condensation mechanism that directs to different morpholo-

gies is presented in Scheme S2. The HR-TEM images of CoMM show graphenic fragments (10−20 nm) entangled together (Figures S10−11). Despite the absence of the nongraphenic structure of CoMM, it demonstrates well-resolved lattice fringes with an interplanar distance of 0.36 nm (Figure 1f). Constrastingly, CoML sheets were mostly amorphous in nature (Figure S12). These findings imply that condensation of planar melem results in better graphitization compared to melamine.

The exceptionally high Co content of CoMM (3.18 at %$_{XPS}$, 10.6 wt %$_{ICP-OES}$) and CoML (2.54 at %$_{XPS}$, 11.13 wt %$_{ICP-OES}$) raised the question of whether Co was present in the nanoparticulate or nanocluster form (Table S3−4). However, the absence of any agglomeration feature in TEM and STEM mapping convinces us to search for the possibility of atomic distribution. We employed aberration-corrected high-angle annular dark-field scanning transmission electron microscopy (AC-HAADF-STEM) to elucidate the ultrafine morphological attributes of CoMM and CoML, which exhibited Co SAs with sharp Z contrasts distributed on the C−N scaffold, and no clusters were observed (Figures 1g,h and S10−11 and S13). Electron energy loss spectroscopy (EELS) mapping of CoMM and CoML at high magnification reveal the uniform distribution of Co and N without any evidence of clustering which implicates that Co is present at the atomic scale. The intense Co and N's EELS signals corroborate densely populated Co−N₄ sites (Figures 1i, S10−11 and S13). Fascinatingly, the EELS spectrum of small pixels of the annular dark field (ADF) image portrayed distinctly visible signals of

Co and N validating the presence of dense Co in the C−N network (Figure 1j). Nevertheless, quantification using EELS showed a high Co content (CoMM-6.4 ± 0.2 and CoML-3.91 ± 0.13 at %); however, after 15 min of continuous beam exposure, we observed damage and clustering, as provided in Table S3 and Figures S14−15. To maintain precision, EELS quantification is not accounted and inductively coupled plasma-optical emission spectroscopy (ICP-OES) which is representative of bulk materials was used as a standard for subsequent studies. The comparison of the relative peak intensity of C K-edge and N K-edge π^* and σ^* transition of CoMM and CoML demonstrate that CoMM possesses a high conjugation degree (sp^2 character) which might be introduced due to lateral fusion of planar structures (Figure S16 and Section 4.0 in SI).[26] Solid-state electron paramagnetic resonance (EPR) spectra of CoMM and CoML do not reveal any signal of ferromagnetic cobalt NPs/clusters at g value ≈2.870. Despite the ferromagnetic nature of single-atom Co^{2+} sites, the absence of any detectable signal was because of their short relaxation time which is in close agreement with previous reports on Co−N$_x$−C SACs.[27] Furthermore, the absence of a broad EPR signal at ≈2.000 g value for CoMM compared to CoML suggests fast relaxation in the ordered π conjugated network while sp^3 defects in CoML delayed the relaxation time (Figure S17 and Section 4.4 in the SI).

The absence of any Co metal-/oxide-related peaks in Raman spectra of CoMM, CoML, and CoGML is ascribed to ultrafine Co distribution (Figure 2a). In contrast, Raman spectra of our control samples (i.e., Co-embedded nanotubular CoCML and CoCMM) displayed sharp vibrational peaks for metallic Co and well-separated D and G bands for the carbonaceous shells.[28] To know the chemical nature of the C−N constituted framework in CoMM and CoML, Raman spectra of carbon black (CB), reduced graphene oxide (RGO), and nitrogen-doped reduced graphene oxide (NRGO) were also measured (Figure S18a and Section 4.5 of the SI). The absence of a 2D band like in NRGO and the presence of broad D and G bands like in CN reported previously suggest the N-rich structure of CoMM and CoML with a periodic arrangement of N atoms.[29] Previous studies also manifested that high-temperature treatment of CN generates C_6N_7 (heptazine) units.[30] The exceptionally high pyridinic N content in XPS and the presence of residual C−N and C_6N_7 signals in FTIR spectra also indicated that the C−N scaffold of CoMM and CoML was created by the direct fusion of C_6N_7 moieties and CoPc (Table S4 and Figure S18b; Section 4.6 in the SI). Moreover, XRD pattern of CoCML and CoCMM displayed (111), (200), and (220) peaks of the metallic α-Co with a face-centered cubic (fcc) structure (Figure 2b).[23,24] The intense (002) peak of stacked graphitic carbon in CoCML and CoCMM insinuates high crystallinity due to better graphitization, in line with HR-TEM results. Interestingly, CoMM and CoML do not show any diffraction peak associated with melem and Co-related species, reinforcing complete condensation of melem and CoPc with atomic Co distribution (Figure S18c and Section 4.7 of SI). CoGML also does not show any nanoparticulated dispersion, and crystalline features due to a high degree of glucose condensation resulted in a dilution of Co sites.

Synchrotron-based wide-angle X-ray scattering (WAXS) allows better spectral resolution and detection limits of crystalline materials on a subnanometric scale. The use of relatively high-energy monochromatic radiation (0.8202 vs 1.5418 Å for CuKα radiation) enables deducing the nano-crystalline attributes and localized crystalline features of the materials (Figure 2c−f).[31] The WAXS 2D map of the CoMM illustrates two broad (002) and (001) diffraction rings at Q values 1.846 and 3.070 Å^{-1} with no further features of any Co/ species, corroborating the absence of nanoscale clustering (Figure 2c,e). In contrast, CoCML delineates many sharp diffraction rings for metallic α-Co and an intense (002) peak of graphitized carbons (Figure 2d,f). The calculated d-spacing of materials was found in the order of CoMM (3.37 Å) < CoCML = CoCMM (3.44 Å) < CoML (3.47 Å) < CoGML (3.64 Å) (Figure S19 and Section 4.8 in the SI). The smallest d-spacing in CoMM, which is close to CN (3.27 Å), emphasizes the partial preservation of the N-rich structure and better graphitization. Regardless of a similar N content, CoML disclosed a relatively high d-spacing, indicating the presence of abundant sp^3 defects compared to CoMM which is aligned with the EELS results.

The elemental composition and type of carbons and nitrogens for each sample are given in Table S4−5. Albeit the use of identical N-rich melem/melamine precursors during synthesis, CoML and CoMM showed an exceptionally high N content (~53 at %) compared to CoCML (3.94 at %) and CoCMM (2.63 at %), supporting direct fusion of C_6N_7 moieties with CoPc at elevated temperatures. The calculated C and N at % of CoMM was 44.69 and 52.13, respectively, which was very close to the theoretical C and N contents of C_6N_7 moieties (C-42.63 and N-57.64 at %), confirming fused C_6N_7 scaffold in CoMM (Figures S20 and S21). Further evidence of intact C_6N_7 nucleus comes from the overlaid C 1s XPS spectra of CoMM and CoML which displayed high N−C≡N/C−N (C−N$_{pyridinic}$) peak contribution matching with reported XPS of CN (Figure 2g and Section 4.9 of SI).[32] The relatively high sp^2 C−C contribution illustrates the removal of bridging Ns during the fusion of C_6N_7 moieties (C−N-0.75 in CN and C−N-0.86 in C_6N_7). The high C−N≡C pyridinic contribution in N1s spectra of CoMM and CoML also supports the fusion of heptazine (C_6N_7) units during the annealing step (Figure 2h). Despite the dominated pyridinic N contribution, the observance of pyrrolic Ns recommends some fraction of C_6N_7 units structurally reorganized during carbonization. Other samples including CoGML, CoCML, and CoCMM show small N−C≡N carbon contribution and high N$_{pyrrolic}$ contribution. This substantiates that carbonization for these materials proceeds through the breaking of melamine/melem moieties followed by graphitization, thus losing significant N content. The Co2p XPS spectra of CoMM and CoML suggest 2+ oxidation state with a broad satellite feature originating from the Co−N contribution in agreement with the previously reported literature (Figure S21c).[33] Interestingly, the XPS spectra of the sample prepared by thermal annealing of CoPc and melem at 600 °C (Co-Mel-600) showed C, N, and O spectra intermediates of CN and CoMM without any trace of Co, suggesting that condensation begins after 600 °C (Figure S22 and Section 4.10 in the SI).

The N K-edge near edge X-ray absorption fine structure (NEXAFS) spectra of CoMM and CoML exhibited a strong $\pi^*_{C−N=C}$ resonance peak along with $\sigma^*_{C−N}$ and $\sigma^*_{C−N=C}$ features matching closely with CN, revealing partial retainment of C_6N_7 signatures (Figure 2i).[34] Intriguingly, the $\pi^*_{N−C3}$ resonance peak originated from the bridging tertiary nitrogen in CN was absent in CoMM and CoML, substantiating that condensation of C_6N_7 moieties proceeds through the removal of bridging nitrogen. The CoGML and CoCMM samples
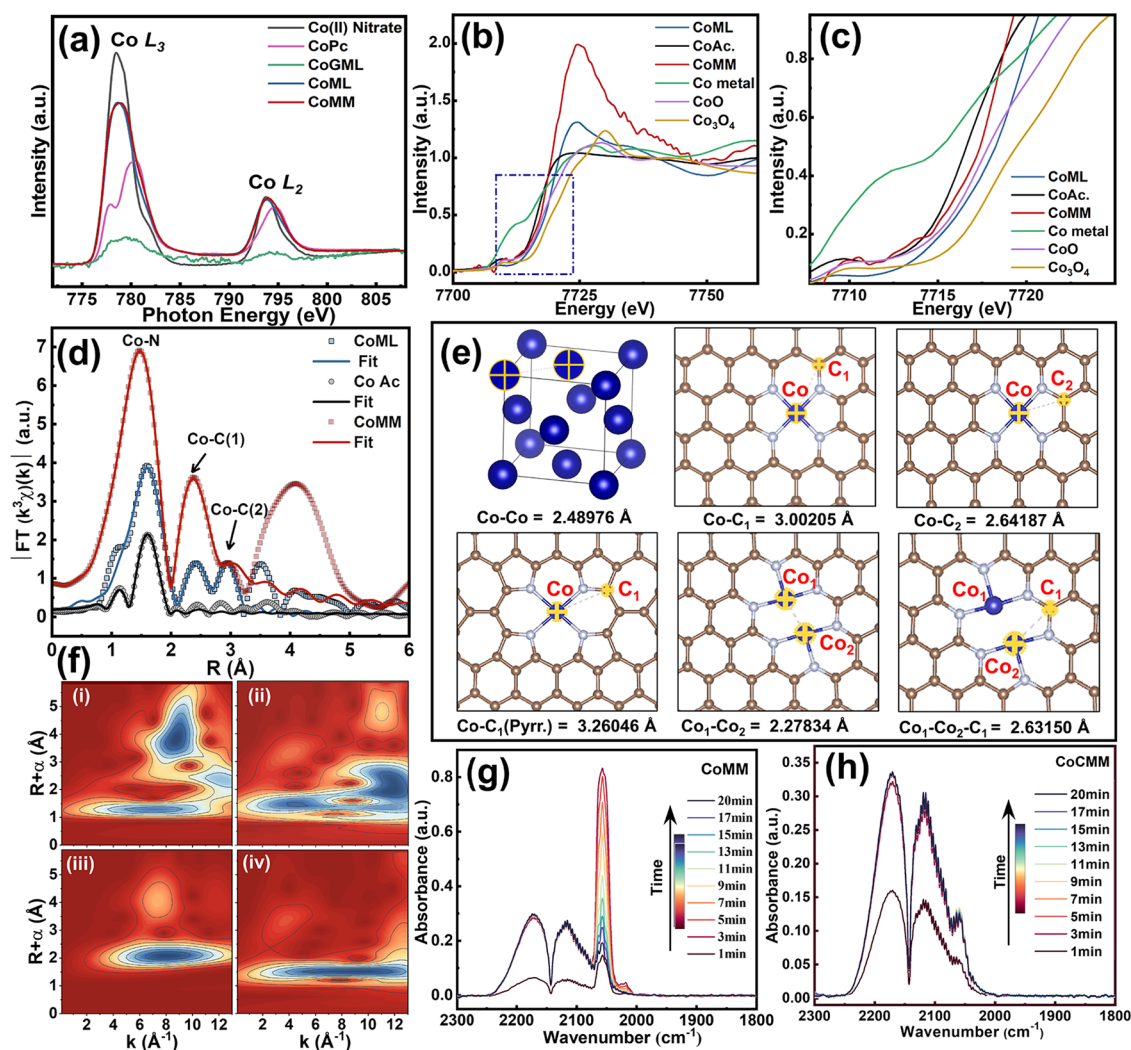
Figure 3. (a) Synchrotron-based soft-X-ray spectra for Co L-edge of Co(II) nitrate, CoPc, CoGML, CoML, and CoMM. (b) XANES spectra of CoML, cobalt acetate, CoMM, metallic Co, CoO, and Co_3O_4. (c) Enlarged XANES spectra of image b. (d) FT-EXAFS spectra of Co Ac. CoML and CoMM. Dots experimental data, Lines-fitted data. (e) DFT simulated models show the distance between neighboring Co−Co (in Co metal and Co dual atom catalyst) and Co−C atoms to correlate with EXAFS results. (f) WT map of (i) CoMM, (ii) CoML, (iii) Co foil, and (iv) Co acetate. Background subtracted CO-DRIFTS time profile spectra of (g) CoMM (h) CoCMM obtained at room temperature.

displayed distinct sp^2 π^*_{C-N} (only for CoGML), $\pi^*_{N(pyridinic)}$, and $\pi^*_{N(pyrrolic)}$ peaks due to N doping in the carbon scaffold (Figure S23 and Section 4.11 of the SI). Like CN, the C K-edge NEXAFS of CoMM and CoML showed an intense $\pi^*_{N-C\equiv N}$ transition peak and only a trace of $\pi^*_{C=C}$ resonance peak was observed which signifies the presence of periodic C−N arrangements (Figure 2j).[35]

To understand the chemical state of Co sites, Co $L_{2,3}$-edge NEXAFS spectra were collected using synchrotron-based soft X-ray radiation. The CoPc $L_{2,3}$-edge NEXAFS spectra exhibited characteristics Co L_3 and L_2 edges of the Co^{2+} state at 780.4 and 794.7 eV due to $2p_{3/2}$, $2p_{1/2} \rightarrow 3d$ transition (Figure 3a and Section 4.12 of SI).[36] The splitting of Co L_3-edges and the appearance of a peak at relatively higher energy demonstrate weak Co−O ligation due to agglomerated μ-oxo state and O/−OH coordination with moisture.[37] The appearance of Co L_3 and Co L_2 edges without any observable splitting in CoMM, CoML, and CoGML unveils the absence of any O coordination, and the CoPc skeleton was destroyed during the annealing step. The appearance of Co L_3 and Co L_2 peaks at a relatively low energy corroborates the efficient

electronic transfer from N to Co in a conjugated graphenic system compared to the 18π ring system of phthalocyanine.

A clearer insight into the Co oxidation state and coordination environment was attained by X-ray absorption near-edge structure (XANES) spectra (Figures 3b,c, S24 and Section 4.13 of the SI). The Co K-edge XANES spectra of CoPc exhibited a characteristic $1s \rightarrow 3d$ transition pre-edge signal at ~7707 eV originating from 3d + 4p mixing in the noncentrosymmetric environment (Figure S24).[38] The intense rising edge and white line transition at ~7713 and ~7724 eV attributed to $1s \rightarrow 4p_z$ and $1s \rightarrow 4p_{x,y}$ transition, revealing the square planer coordination of Co^{2+}.[39] The XANES spectra of CoMM and CoML showed a sharp $1s \rightarrow 4p$ transition edge closer to the CoO inferring the 2+ oxidation state (Figure 3c).[40] The absence of any pre-edge feature and sharp rising edge are related to a centrosymmetric square planer structure of the cobalt centers. The absence of any CoPc clone features and the appearance of an intense white line in CoMM indicate the fusion of the CoPc macrocyclic ring followed by the formation of square planar N-coordinated Co SA sites in the graphenic structure.[41] The broad and nonspecific XANES
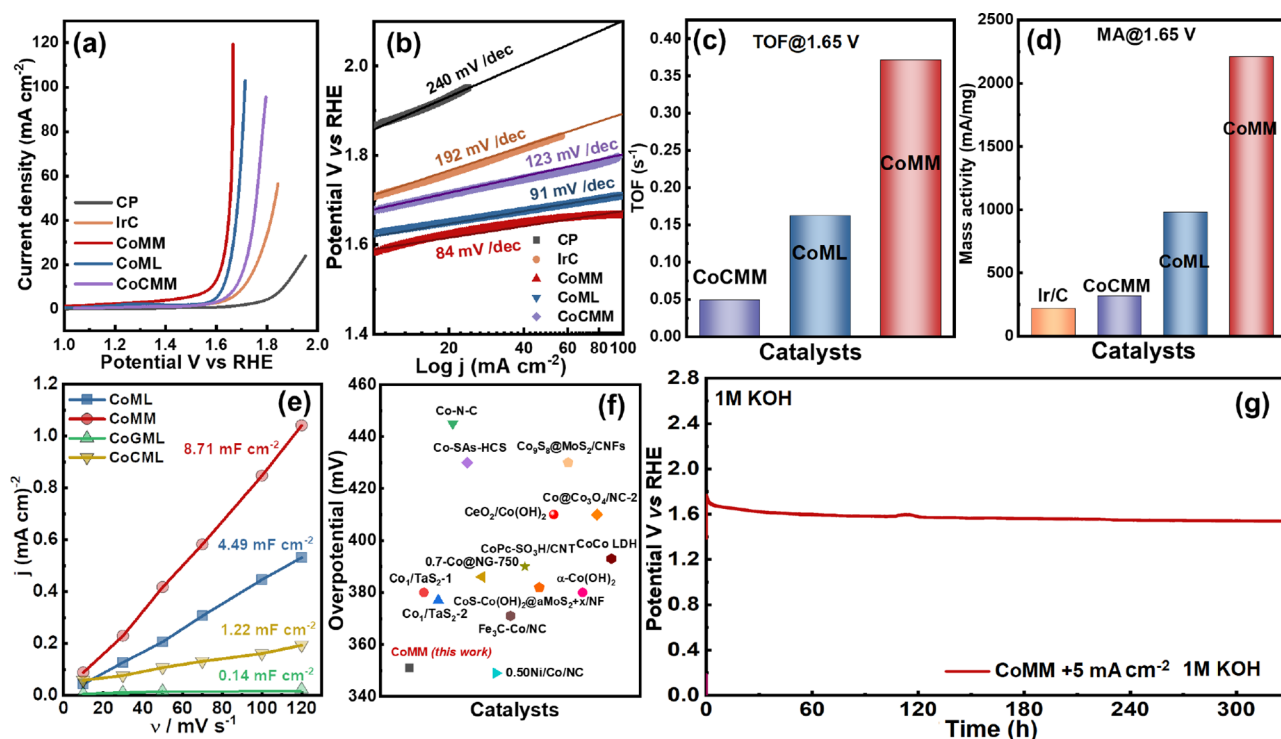
Figure 4. Electrocatalytic OER performance of Co-based electrodes (CP: carbon paper). (a) OER LSV study at 5 mV S^{-1}. (b) Tafel slopes. (c) TOF at 1.65 V. (d) Mass activity. (e) C_{dl} values from ΔJ vs ν in a non-Faradaic region. (f) Comparison of OER activities (@10 mA cm^{-2}) of CoMM with other catalysts. (g) Long-term stability of CoMM for 300 h at 5 mA cm^{-2}.

profile observed for the CoGML reveals mixed oxidation state Co sites which were also evidenced from Co L-edge NEXAFS spectra (Figure S24). Interestingly, the CoCMM prepared using metal salt displayed a Co K-edge that matches with metallic Co, validating encased metallic cobalt in the carbon scaffold (Figure S24).

To illustrate the atomic coordination environment of Co sites in the materials, Fourier-transform extended X-ray absorption fine structure (FT-EXAFS) spectra were acquired (Figure 3d). The EXAFS of CoMM displayed a sharp first coordination shell at 1.472 Å that originated from the Co−N scattering, which is aligned with Co L-edges in NEXAFS spectra. Additionally, a second coordination shell at 2.377 Å with a shoulder peak at 2.978 Å appeared due to the Co−N−C scattering. It should be noted that, due to high Co concentrations, the Co−N−C second shell scattering was intense which agreed well with previously reported high metal-containing SACs.[42,43] To further examine the origin of the second coordination shell and whether Co was present in the pyridinic or pyrrolic cavity, the obtained bond lengths were compared using different models (Figure 3e). It can be seen from the model that the metallic Co−Co (2.489 Å) and Co-C$_1$ pyrrolic (3.260 Å) distance was significantly higher than our experimental value, excluding the possibility of any metallic and pyrrolic contribution. Some reports also demonstrate the origin of second coordination shells from dual atomic sites[44,45] however, the calculated Co−Co distance in the dual-site model was just 2.278 Å, corroborating the absence of any such interactions. These observations indicate the presence of isolated Co coordinated to the pyridinic N framework. However, we also observed relatively small pyrrolic Ns contribution in XPS; thus, pure Co−N$_{pyridinic}$ structures cannot be claimed, and signals will be an average contribution of each

entity. EXAFS data fitting of CoMM for both first and second coordination shells demonstrated Co−N and Co−C coordination numbers (CNs) of 3.99 ($\pm$0.04) and 3.87 ($\pm$0.08) with a bond length of 2.01 and 2.62 Å, respectively (Table S6). The second shell bond length closely matched with the pyridinic model, validating the Co−N$_4$C$_4$ moieties embedded in the graphenic structure. As expected, CoML also demonstrated identical features, except Co−C$_1$ scattering was slightly less intense (CN-3.41 $\pm$ 0.09), suggesting the presence of few defect states aligned with EELS and EPR observations.

To further clarify the neighbor structure around Co atoms, wavelet transform (WT) EXAFS spectra of CoMM, CoML, Co foil, and Co acetate were calculated. As shown in Figure 3f, cobalt foil shows an obvious sharp zone in K = 8.16 Å^{-1} and R = 2.09 Å that represents Co−Co metal bonds. Compared to the standard Co foil samples, CoMM, CoML, and Co acetate do not display similar sharp zones in the same position, which indicates that these three samples do not contain a Co−Co metal bond. Generally, in the lower position of K space and R space, this sharp zone is assigned as the first shell of Co−N. The sharp zone in the high position of K space and R space stems from the second shell scattering.[46] Moreover, CoMM and CoML display a sharp zone at 12 Å^{-1} in the high K space position, and their R space position in this zone was about 2.39 Å. Therefore, this sharp zone can be considered as the second shell Co−N−C scattering in these single-atom catalysts, which is consistent with the reported studies.[42]

To probe the uniform isolated site distribution, diffuse reflectance infrared Fourier-transform spectroscopy (DRIFTS) profiles were recorded as a function of time. The DRIFTS spectra of CO-unprobed samples indicate close similarity of CoGML/CoCMM surfaces while CoMM/CoML demonstrate bands like carbon nitride which was also observed in FTIR and
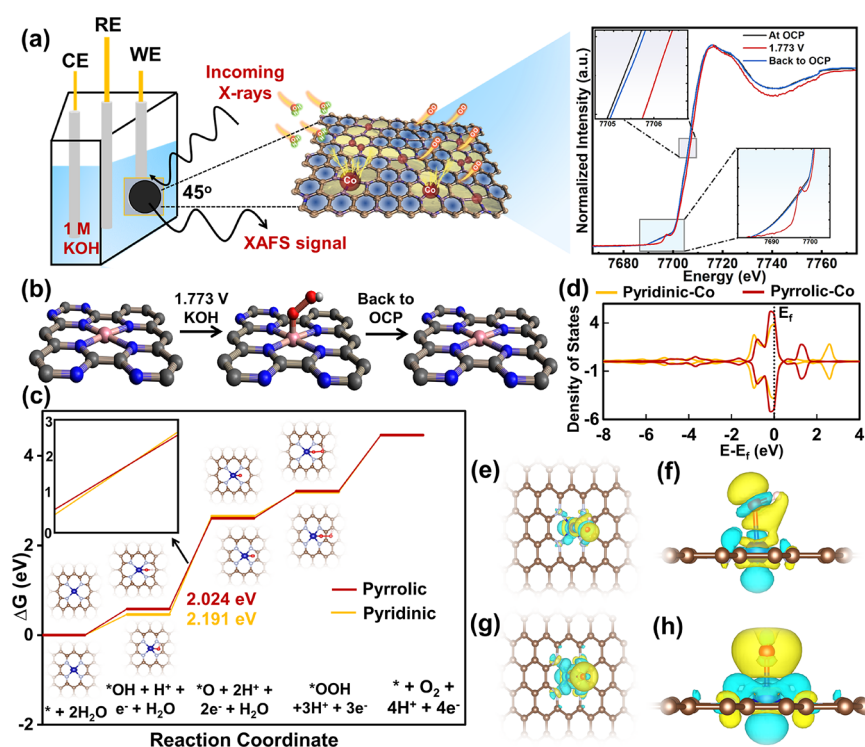
Figure 5. (a) Schematics of operando XAS analysis of CoMM: XANES spectra at OCV and 1.773 V vs RHE. (b) Chemical state change of CoMM during OER showing the regeneration of the active sites. (c) OER free energy profile of pyridinic-nitrogen–cobalt (representing CoMM and CoML) and pyrrolic-nitrogen–cobalt single-atom models. Cobalt, carbon, nitrogen, oxygen, and hydrogen atoms are marked as blue, brown, gray, red, and pink, respectively. Orange highlight represents the RDSs with the values of the relevant energy barriers labeled. (d) PDOS on the Co atom for both pyridinic-nitrogen–cobalt and pyrrolic-nitrogen–cobalt single-atom models. Electron density difference for *OH and *O intermediates on the pyridinic model. (e) Top view and (f) side view of *OH. (g) Top view and (h) side view of *O.

Raman spectra (Figure S25). The observed similarities in vibrational spectra originated from the precursors which provide a specific C−N backbone. The CO-DRIFTS spectra of all Co samples exhibited two board bands at 2115 and 2174 cm^{-1} attributed to the residual CO species adsorbed on the support matrix (Figures 3g,h and S25). However, DRIFTS spectra of CoMM and CoML in the lower frequency region displayed three isolated peaks at 2063, 2056, and 2047 cm^{-1}, respectively, which might originate from the weak interaction of CO with the isolated Co atom grafted on the N−C scaffold (Figures 3g and S25).[47] A closer look reveals that with the course of CO purging, the overlap peak intensity centered around 2065−2045 cm^{-1} diminished, which implies the complete saturation of Co SA sites by the CO probe molecule, leading to a gradual reduction of the peak intensity (Figures 3g and S25).[48] These observations suggest that upon CO adsorption, all the distributed Co sites were saturated after entailing with CO-probe molecules. The saturated sites leave no single atomic sites available to further accommodate CO adsorption, indicating the presence of dispersed and isolated Co-atom sites on the catalyst. On the other hand, CO-DRIFTS spectra of CoGML and CoCMM were significantly different from the CoMM and CoML catalysts and did not show any similarity with Co−N surface characterization. Since the metal content in CoGML was significantly low, major signals can be expected to arise from the carbonaceous scaffold (Figure S25). In the case of CoCMM, metallic Co was embedded in graphitized carbon nanotubes; therefore, Co sites remain unexposed to bind with CO molecules and do not show any appreciable change in DRIFTS spectra.

Electrocatalytic OER (1.0 M KOH) Studies. Electrocatalytic OER studies were carried out in O_2-saturated 1.0 M KOH. When OER was evaluated from linear sweep voltammetry (LSV), CoMM offered the lowest η_{10} values of 351 mV as compared to CoML (395 mV), CoCMM (446 mV), and benchmark Ir/C (494 mV) catalysts (Figure 4a). Kinetic parameters from the Tafel slope (log j vs η) exhibit the lowest value for CoMM (84 mV/dec) (Figures 4b and S26). Evidently, CoMM SACs undergo OER with facile kinetics compared to other Co counterparts due to maximum site availability. Electrochemical impedance spectroscopy (EIS) spectra at 393 mV show low R_{ct} (charge transfer resistance) for CoMM (13 Ω) compared to benchmark Ir/C (54 Ω), CoML (146 Ω), and Pt/C (418 Ω), which is aligned with the polarization and Tafel results (Figure S27).[49] CoMM exhibited a very high turnover frequency (TOF) of 0.37 O_2 per Co site per second, at 420 mV, showcasing its high intrinsic activity compared to CoML (0.15 O_2 per Co site per second) (Figure 4c). The mass activity was found to be significantly high in CoMM (2209 mA mg$_{Co}^{-1}$) (Figure 4d) and its superior OER performance is also reflected in terms of j vs η, as depicted in Figure S28. We further measured double-layer capacitance (C_{dl}) to evaluate the electrochemical surface area (ECSA) of Co SACs (Figure S29a−e). We found a C_{dl} of 8.71 mF cm^{-2} for CoMM, almost double that of CoML (4.49 mF cm^{-2}), resulting in ECSA values of 218 and 112 real/cm^2, respectively, which is consistent with N_2 isotherm results (Figures 4e and S6). Specific activities from ECSA normalization show enhanced OER activity of CoMM compared to CoML and a similar trend was observed in mass activity and TOF values (Figure S30a−c).[50] The comparison of CoMM's activity with

related M−N$_x$−C, hydroxides, and layered double hydroxides (LDHs) denotes the role of populated Co atoms and their influence on OER (Figure 4f). It is worth mentioning that high-density N carbon/graphene-based electrocatalysts (>10% loading) derived from metal−organic frameworks (MOFs), metal-implanted quantum dots, and multiple-step annealing are only explored for ORR and electrochemical CO$_2$ reduction reaction (eCO$_2$RR) (Figure S31 and Table S7). The impedance measured at OCP and (0.5 to 0.7 V) vs Ag/AgCl display semicircle arc was shrunk with rising potentials (Figure S32). This implies that the Co−N$_4$ coordination in SACs as well as the pyridinic scaffold with strong $\pi-\pi^*$ delocalization ameliorates O-adsorption/desorption kinetics.[51] A closer look at Figure S32a−e conveys that CoMM requires a lesser potential drive for the O-containing intermediates compared to Ir/C and CoML catalysts.

The electrochemical stability of electrodes for long-term operation conditions was analyzed via chronopotentiometric study in alkaline (OER) electrolytes. Initially, the stability of CoMM and CoML was analyzed at 10 mA cm^{-2} for 16 h which showed negligible degradation in activity for OER (Figure S33).[52] Figure 4g displays long-term chronopotentiometry of CoMM at 5 mA cm^{-2} which showed negligible potential drop even up to 300 h of continuous electrolysis. Similarly, CoML appears to have constant stability and extended stability for 200 h at 5 mA cm^{-2} during OER (Figure S34). We executed post-OER EIS analysis of CoMM and compared it with other Co-counterparts. Considering post-OER EIS of the CoMM catalyst, the change in R_{ct} was significantly small, implying high-scale activity and stability of CoMM for OER (Figure S35a). A similar trend was observed in CoML as well; however, R_{ct} was higher, as depicted in Figure S35b.[7] The ICP-OES analysis of the electrolyte after OER at 5, 10 mA cm^{-2} for 16 h and 500 CV cycles at 100 mV s^{-1} using the CoMM electrode does not show any trace of Co, corroborating that Co SA species were stably ligated to N-rich carbonaceous framework (Table S8 and Section 4.14 in SI). Furthermore, XPS analysis of the CoMM electrode after OER reveals the absence of any significant changes in C 1s and N 1s spectra; however, Co 2p spectra displayed the evolution of Co^{3+} species (CoOOH), suggesting that hypervalent Co^{3+} participates in OER (Figure S36 and Section 4.15 in the SI). As expected, post-OER Raman analysis does not display any CoOOH signals due to the atomic distribution of CoOOH species in the carbonaceous framework (Figure S37 and Section 4.16 in the SI). From the overall OER results, CoMM was found to deliver the best activity and stability, proving that its high atomic Co% and $\pi-\pi^*$ delocalization electron density play a significant role in the noteworthy performance compared to other catalysts.[11] To ensure that the generated current was purely electrocatalytic and not due to degradation of the carbonaceous scaffold, we collected the gaseous samples which show O$_2$ as a prime component and do not show any trace of CO and CO$_2$, validating the stable nature of the catalysts (Figure S38)

Operando XAS Analysis and DFT Studies. We conducted operando X-ray absorption spectroscopy (XAS) analysis to elucidate the dynamic role of active sites in CoMM by comparing the real-time change in the Co chemical state between OCP and 1.773 V vs RHE in the OER region (Figures 5a and S39). The Co K-edge spectra at OCP demonstrate a sharp rising edge due to 1s → 4p transition while 1s to 3d dipole-forbidden transitions were almost absent, demonstrating

a high plane D$_{4h}$/S$_4$ symmetry and a square planar Co−N$_4$ structure.[53] The rising edge and white line intensity of CoMM was identical to ex-situ measurements (Figure 3c), demonstrating that the Co^{2+} square planar structure of CoMM remains unaltered in the KOH electrolyte. When the potential bias is applied, Co^{2+} is slightly oxidized to Co$^{2+\delta+}$ due to the oxy-hydroxide formation, which is evident from the positive shift of the 1s → 4p peak. Furthermore, the emergence of a strong pre-edge feature is attributed to the forbidden 1s → 3d transition of unfilled 3d orbitals when O is coordinated to the Co edge sites. This pre-edge feature manifests distortion of the centrosymmetric structure due to Co−O bonding. Upon reversing the potential to OCP, the XANES spectrum reverts back to the initial state, indicating the regeneration of the active site for another −OH adsorption (Figure 5b). From the operando XAS analysis, certainly, the pyridinic-nitrogen−cobalt sites in the CoMM are highly pronounced toward OER with superior activity and regenerability. As the nature of size and spacing strongly influence the OER activity, we analyzed the spacing between Co−Co single atoms (d$_{Co−Co}$) by employing high-magnification HAADF images. As pictured in Figure S40, the spacing between two neighboring Co−Co atoms was calculated to be ∼3.85 Å, revealing the densely populated Co sites in CoMM. To further validate the obtained spacing, we calculated d$_{Co−Co}$ using at % XPS and Brunauer−Emmett−Teller (BET) surface area which showed ∼3.85 Å d$_{Co−Co}$, indicating vicinal Co decoration (Table S9).[54] Previously, Jin et al. demonstrated that the distance between two neighboring Fe−Fe atoms in graphenic scaffold directly affects ORR performance as the d$_{Fe−Fe}$ falls below 1.8 nm due to the remarkable decrease in the magnetic moment and facile M$_{3d}$−O$_{2p}$ interaction.[55] In this context, here, densely populated CoMM with smaller d$_{Co−Co}$ and feasible, e$_g$ filling improves OER activity. From the overall electrocatalytic and in-situ structural studies, CoMM has outperformed others in terms of dense Co sites, optimum d$_{Co−Co}$, and abundant pyridinic structures.

To evaluate whether pyridinic sites are ideal to afford the highest OER performance, we intended to compare them with pyrrolic sites as well. To compare pyridinic CoMM/CoML with potentially synthesizable pyrrolic-nitrogen−cobalt single-atom catalysts, we carried out the following DFT studies. As depicted in Figure 5c, the M-OH adsorption is more favorable in the pyridinic structure compared to the pyrrolic structure. From the M-OOH formation which is a rate-determining step (RDS), the pyrrolic-nitrogen−cobalt (2.024 eV) demonstrates a comparable energy barrier compared to pyridinic-nitrogen−cobalt (2.191 eV). The reaction mechanisms as well as the reaction intermediates for both SA models are illustrated in Figures S41−42, while the energy values of different adsorption systems are summarized in Table S10. These observations suggest that pyrrolic-nitrogen−cobalt sites (if synthesizable) might deliver a slightly better OER than pyridinic-nitrogen−cobalt sites. However, the synthesized pyrrolic-nitrogen-rich catalysts (CoGML, CoCML, and CoCMM) contain either a substantially lower Co content or metallic Co NPs, thus displaying inferior performance. To verify this, the projected density of states (PDOS) on Co in pyrrolic and pyridinic-nitrogen−cobalt SA models was also constructed (Figure 5d). PDOS indicates that the pyrrolic one possesses a d-band center closer to the Fermi level, leading to stronger bonding between the oxygenated adsorbates and Co compared to the pyridinic model.[56] Bader charge analysis and

the charge density difference plots for the *OH and *O intermediates at the RDS (Figures 5e−h and S43−44) demonstrate that the pyrrolic structure enhances electron transfer from cobalt to oxygen for *OH. However, the electron transfer for *O was similar in both pyridinic and pyrrolic models. A similar trend was also observed in the charge density difference plots, where the electron transfer from cobalt to oxygen is larger (i.e., the cyan and yellow regions are more separate) for *OH on the pyrrolic structure (Figure S44a,b) compared with the pyridinic structure (Figure 5e,f), while the charge density difference plots remain similar for *O in both structures. Therefore, our DFT results demonstrate comparable performance in both pyridinic and pyrrolic Co SACs and posit feasibility of slight improvements for the pyrrolic structure.

■ CONCLUSIONS

In summary, this work describes an improved synthesis protocol of high-density Co SA sites (10.6 wt %) in pyridinic N-rich graphenic networks using planar CoPc and melem monomers. The direct fusion of melem's C_6N_7 units and CoPc yielded Co SA sites stabilized in a N-rich conjugated carbonaceous scaffold, actuating better charge transport during electrocatalysis. The synchrotron-based WAXS eliminates the occurrence of any subnanometric clustering while the fitting of scattering data confirms pyridinic Co−N_4 entities embedded on the carbonaceous scaffold. The isolated Co center promotes highly efficient and stable (>300 h) electrocatalytic OER. With synergistic metal−support interactions, the catalysts can reach a mass activity/TOF as high as 2209 mA mg_{Co}^{-1} at 1.65 V/ 0.37 s^{-1}. Operando XANES analysis probed the facile formation of an electron-deficient Co−O intermediate state. Bader charge analysis, density of states, and DFT studies reveal that Co−N_4 SACs are potential candidates for the OER in terms of lower free energy changes and favorable electronic transport. These findings may inspire research in the rational design of high-concentration OER SA electrocatalysts to replace noble metal-based catalysts. Beyond electrocatalysis, the extension of the devised synthetic protocol will also enable fabrication of other high-density metallic SACs to catalyze state-of-the-art reactions at the industrial scale.

■ ASSOCIATED CONTENT

Ⓢ Supporting Information

The Supporting Information is available free of charge at https://pubs.acs.org/doi/10.1021/jacs.3c00537.

> Experimental details (materials and characterization); synthesis; FE-SEM, HR-TEM, AC-HAADF STEM, EELS, WAXS, XPS, XRD, Raman, and FTIR spectroscopy; N_2 adsorption−desorption isotherm; soft X-ray, XANES, EXAFS, EPR, and CO-DRIFT spectroscopy; electrochemical measurements (LSV, Tafel, ECSA, EIS, and chronopotentiometry); GC chromatograms; operando XANES setup; and DFT analysis (PDF)

■ AUTHOR INFORMATION

Corresponding Authors

Pawan Kumar − *Department of Chemical and Petroleum Engineering, University of Calgary, Calgary, Alberta T2N 1N4, Canada;* ⊙ orcid.org/0000-0003-2804-9298; Email: pawan.kumar@ucalgary.ca

Jinguang Hu − *Department of Chemical and Petroleum Engineering, University of Calgary, Calgary, Alberta T2N 1N4, Canada;* ⊙ orcid.org/0000-0001-8033-7102; Email: jinguang.hu@ucalgary.ca

Md Golam Kibria − *Department of Chemical and Petroleum Engineering, University of Calgary, Calgary, Alberta T2N 1N4, Canada;* ⊙ orcid.org/0000-0003-3105-5576; Email: md.kibria@ucalgary.ca

Authors

Karthick Kannimuthu − *Department of Chemical and Petroleum Engineering, University of Calgary, Calgary, Alberta T2N 1N4, Canada*

Ali Shayesteh Zeraati − *Department of Chemical and Petroleum Engineering, University of Calgary, Calgary, Alberta T2N 1N4, Canada*

Soumyabrata Roy − *Department of Materials Science and NanoEngineering, Rice University, Houston, Texas 77030, United States;* ⊙ orcid.org/0000-0003-3540-1341

Xiao Wang − *Department of Chemical Engineering, McGill University, Montreal, Quebec H3A 0C5, Canada; Present Address: Department of Chemical Engineering, Massachusetts Institute of Technology, Cambridge, Massachusetts 02139, United States (X.W.);* ⊙ orcid.org/0000-0003-1624-8230

Xiyang Wang − *Department of Mechanical and Mechatronics Engineering, Waterloo Institute for Nanotechnology, Materials Interface Foundry, University of Waterloo, Waterloo, Ontario N2L 3G1, Canada;* ⊙ orcid.org/0000-0002-7591-6676

Subhajyoti Samanta − *Department of Chemical and Biomolecular Engineering, Lehigh University, Bethlehem, Pennsylvania 18015, United States; Present Address: Department of Chemical Sciences (DCS), Tata Institute of Fundamental Research (TIFR), Mumbai 400005, India (S.S.)*

Kristen A. Miller − *Department of Materials Science and NanoEngineering, Rice University, Houston, Texas 77030, United States;* ⊙ orcid.org/0000-0002-5694-3169

Maria Molina − *Department of Chemical and Petroleum Engineering, University of Calgary, Calgary, Alberta T2N 1N4, Canada; Department of Chemistry, University of Calgary, Calgary, Alberta T2N 1N4, Canada*

Dhwanil Trivedi − *Department of Chemical and Petroleum Engineering, University of Calgary, Calgary, Alberta T2N 1N4, Canada*

Jehad Abed − *Department of Electrical and Computer Engineering, University of Toronto, Toronto, Ontario M5S 3G4, Canada;* ⊙ orcid.org/0000-0003-1387-2740

M. Astrid Campos Mata − *Department of Materials Science and NanoEngineering, Rice University, Houston, Texas 77030, United States*

Hasan Al-Mahayni − *Department of Chemical Engineering, McGill University, Montreal, Quebec H3A 0C5, Canada*

Jonas Baltrusaitis − *Department of Chemical and Biomolecular Engineering, Lehigh University, Bethlehem, Pennsylvania 18015, United States;* ⊙ orcid.org/0000-0001-5634-955X

George Shimizu − *Department of Chemistry, University of Calgary, Calgary, Alberta T2N 1N4, Canada;* ⊙ orcid.org/0000-0003-3697-9890

Yimin A. Wu − *Department of Mechanical and Mechatronics Engineering, Waterloo Institute for Nanotechnology,*

Materials Interface Foundry, University of Waterloo, Waterloo, Ontario N2L 3G1, Canada; ● orcid.org/0000-0002-3807-8431

Ali Seifitokaldani − Department of Chemical Engineering, McGill University, Montreal, Quebec H3A 0C5, Canada; ● orcid.org/0000-0002-7169-1537

Edward H. Sargent − Department of Electrical and Computer Engineering, University of Toronto, Toronto, Ontario M5S 3G4, Canada; ● orcid.org/0000-0003-0396-6495

Pulickel M. Ajayan − Department of Materials Science and NanoEngineering, Rice University, Houston, Texas 77030, United States; ● orcid.org/0000-0001-8323-7860

Author Contributions

○K.K. and A.S.Z. have contributed equally.

Notes

The authors declare no competing financial interest.

■ REFERENCES

(1) Feldman, D.; Ramasamy, V.; Fu, R.; Ramdas, A.; Desai, J.; Margolis, R. US Solar Photovoltaic System and Energy Storage Cost Benchmark (Q1 2020); National Renewable Energy Lab.(NREL): Golden, CO (United States), 2021.

(2) Birdja, Y. Y.; Pérez-Gallent, E.; Figueiredo, M. C.; Göttle, A. J.; Calle-Vallejo, F.; Koper, M. Advances and Challenges in Understanding the Electrocatalytic Conversion of Carbon Dioxide to Fuels. Nat. Energy 2019, 4, 732−745.

(3) You, B.; Sun, Y. Innovative Strategies for Electrocatalytic Water Splitting. Acc. Chem. Res. 2018, 51, 1571−1580.

(4) Shan, J.; Ye, C.; Chen, S.; Sun, T.; Jiao, Y.; Liu, L.; Zhu, C.; Song, L.; Han, Y.; Jaroniec, M.; Zhu, Y.; Zheng, Y.; Qiao, S. Z. Short-Range Ordered Iridium Single Atoms Integrated into Cobalt Oxide Spinel Structure for Highly Efficient Electrocatalytic Water Oxidation. J. Am. Chem. Soc. 2021, 143, 5201−5211.

(5) Shan, J.; Ye, C.; Zhu, C.; Dong, J.; Xu, W.; Chen, L.; Jiao, Y.; Jiang, Y.; Song, L.; Zhang, Y.; Jaroniec, M.; Zhu, Y.; Zheng, Y.; Qiao, S. Z. Integrating Interactive Noble Metal Single-Atom Catalysts into Transition Metal Oxide Lattices. J. Am. Chem. Soc. 2022, 144, 23214−23222.

(6) Zhao, J.; Ji, S.; Guo, C.; Li, H.; Dong, J.; Guo, P.; Wang, D.; Li, Y.; Toste, F. D. A Heterogeneous Iridium Single-Atom-Site Catalyst for Highly Regioselective Carbenoid O−H Bond Insertion. Nat. Catal. 2021, 4, 523−531.

(7) Kumar, P.; Al-Attas, T.; Hu, J.; Kibria, M. G. Single Atom Catalysts for Selective Methane Oxidation to Oxygenates. ACS Nano 2022, 16, 8557−8618.

(8) Fei, H.; Dong, J.; Chen, D.; Hu, T.; Duan, X.; Shakir, I.; Huang, Y.; Duan, X. Single Atom Electrocatalysts Supported on Graphene or Graphene-Like Carbons. Chem. Soc. Rev. 2019, 48, 5207−5241.

(9) Rong, X.; Wang, H. J.; Lu, X. L.; Si, R.; Lu, T. B. Controlled Synthesis of a Vacancy-Defect Single-Atom Catalyst for Boosting CO2 Electroreduction. Angew. Chem., Int. Ed. 2020, 59, 1961−1965.

(10) Wu, Z.-Y.; Karamad, M.; Yong, X.; Huang, Q.; Cullen, D. A.; Zhu, P.; Xia, C.; Xiao, Q.; Shakouri, M.; Chen, F.-Y.; Kim, J. Y.; Xia, Y.; Heck, K.; Hu, Y.; Wong, M. S.; Li, Q.; Gates, I.; Siahrostami, S.; Wang, H. Electrochemical Ammonia Synthesis via Nitrate Reduction on Fe Single Atom Catalyst. Nat. Commun. 2021, 12, 2870.

(11) Zhang, L.; Jia, Y.; Gao, G.; Yan, X.; Chen, N.; Chen, J.; Soo, M. T.; Wood, B.; Yang, D.; Du, A. Graphene Defects Trap Atomic Ni Species for Hydrogen and Oxygen Evolution Reactions. Chem 2018, 4, 285−297.

(12) Fei, H.; Dong, J.; Feng, Y.; Allen, C. S.; Wan, C.; Volosskiy, B.; Li, M.; Zhao, Z.; Wang, Y.; Sun, H.; An, P.; Chen, W.; Guo, Z.; Lee, C.; Chen, D.; Shakir, I.; Liu, M.; Hu, T.; Li, Y.; Kirkland, A. I.; Duan, X.; Huang, Y. General Synthesis and Definitive Structural Identification of MN4C4 Single-Atom Catalysts with Tunable Electrocatalytic Activities. Nat. Catal. 2018, 1, 63−72.

(13) Shan, J.; Ye, C.; Jiang, Y.; Jaroniec, M.; Zheng, Y.; Qiao, S.-Z. Metal-Metal Interactions in Correlated Single-Atom Catalysts. Sci. Adv. 2022, 8, No. eabo0762.

(14) Zhao, L.; Zhang, Y.; Huang, L.-B.; Liu, X.-Z.; Zhang, Q.-H.; He, C.; Wu, Z.-Y.; Zhang, L.-J.; Wu, J.; Yang, W.; Gu, L.; Hu, J. S.; Wan, L. J. Cascade Anchoring Strategy for General Mass Production of High-Loading Single-Atomic Metal-Nitrogen Catalysts. Nat. Commun. 2019, 10, 1278.

(15) Zou, L.; Wei, Y. S.; Hou, C. C.; Li, C.; Xu, Q. Single-Atom Catalysts Derived from Metal−Organic Frameworks for Electrochemical Applications. Small 2021, 17, 2004809.

(16) Wu, J.; Zhou, H.; Li, Q.; Chen, M.; Wan, J.; Zhang, N.; Xiong, L.; Li, S.; Xia, B. Y.; Feng, G.; Liu, M.; Huang, L. Densely Populated Isolated Single Co−N Site for Efficient Oxygen Electrocatalysis. Adv. Energy Mater. 2019, 9, 1900149.

(17) Liu, W.; Chen, Y.; Qi, H.; Zhang, L.; Yan, W.; Liu, X.; Yang, X.; Miao, S.; Wang, W.; Liu, C. A Durable Nickel Single-Atom Catalyst for Hydrogenation Reactions and Cellulose Valorization Under Harsh Conditions. Angew. Chem., Int. Ed. 2018, 57, 7071−7075.

(18) Sun, T.; Zhao, S.; Chen, W.; Zhai, D.; Dong, J.; Wang, Y.; Zhang, S.; Han, A.; Gu, L.; Yu, R.; Wen, X.; Ren, H.; Xu, L.; Chen, C.; Peng, Q.; Wang, D.; Li, Y. Single-Atomic Cobalt Sites Embedded in Hierarchically Ordered Porous Nitrogen-Doped Carbon as a Superior Bifunctional Electrocatalyst. Proc. Natl. Acad. Sci. U. S. A. 2018, 115, 12692−12697.

(19) Li, B. Q.; Zhao, C. X.; Chen, S.; Liu, J. N.; Chen, X.; Song, L.; Zhang, Q. Framework-Porphyrin-Derived Single-Atom Bifunctional Oxygen Electrocatalysts and Their Applications in Zn−Air Batteries. Adv. Mater. 2019, 31, 1900592.

(20) Xia, C.; Qiu, Y.; Xia, Y.; Zhu, P.; King, G.; Zhang, X.; Wu, Z.; Kim, J. Y. T.; Cullen, D. A.; Zheng, D.; Li, P.; Shakouri, M.; Heredia, E.; Cui, P.; Alshareef, H. N.; Hu, Y.; Wang, H. General Synthesis of Single-Atom Catalysts with High Metal Loading Using Graphene Quantum Dots. Nat. Chem. 2021, 13, 887−894.

(21) Zhao, X.; Zhao, Y.; Tan, H.; Sun, H.; Qin, X.; Ho, W.; Zhou, M.; Lin, J.; Li, Y. New Carbon Nitride Close to C$_6$N$_7$ with Superior Visible Light Absorption for Highly Efficient Photocatalysis. *Sci. Bull.* **2021**, *66*, 1764−1772.

(22) Bafekry, A.; Faraji, M.; Fadlallah, M.; Abdolhosseini Sarsari, I.; Jappor, H.; Fazeli, S.; Ghergherehchi, M. Two-Dimensional Porous Graphitic Carbon Nitride C$_6$N$_7$ Monolayer: First-Principles Calculations. *Appl. Phys. Lett.* **2021**, *119*, 142102.

(23) Zou, X.; Huang, X.; Goswami, A.; Silva, R.; Sathe, B. R.; Mikmeková, E.; Asefa, T. Cobalt-Embedded Nitrogen-Rich Carbon Nanotubes Efficiently Catalyze Hydrogen Evolution Reaction at All pH Values. *Angew. Chem.* **2014**, *126*, 4461−4465.

(24) Yang, Z.; Zhao, C.; Qu, Y.; Zhou, H.; Zhou, F.; Wang, J.; Wu, Y.; Li, Y. Trifunctional Self-Supporting Cobalt-Embedded Carbon Nanotube Films for ORR, OER, and HER Triggered by Solid Diffusion from Bulk Metal. *Adv. Mater.* **2019**, *31*, 1808043.

(25) Kang, J.; Zhou, L.; Duan, X.; Sun, H.; Ao, Z.; Wang, S. Degradation of Cosmetic Microplastics via Functionalized Carbon Nanosprings. *Matter* **2019**, *1*, 745−758.

(26) Axen, N.; Botton, G.; Somekh, R.; Hutchings, I. Effect of Deposition Conditions on the Chemical Bonding in Sputtered Carbon Nitride Films. *Diamond Relat. Mater.* **1996**, *5*, 163−168.

(27) Li, X.; Surkus, A. E.; Rabeah, J.; Anwar, M.; Dastigir, S.; Junge, H.; Brückner, A.; Beller, M. Cobalt Single-Atom Catalysts with High Stability for Selective Dehydrogenation of Formic Acid. *Angew. Chem., Int. Ed.* **2020**, *59*, 15849−15854.

(28) Kotal, M.; Sharma, A.; Jakhar, S.; Mishra, V.; Roy, S.; Sahoo, S. C.; Sharma, H. K.; Mehta, S. K. Graphene-Templated Cobalt Nanoparticle Embedded Nitrogen-Doped Carbon Nanotubes for Efficient Visible-Light Photocatalysis. *Cryst. Growth Des.* **2020**, *20*, 4627−4639.

(29) Chowdhury, A.; Cameron, D. C.; Hashmi, M. Vibrational Properties of Carbon Nitride Films by Raman Spectroscopy. *Thin Solid Films* **1998**, *332*, 62−68.

(30) Zhao, Y.; Liu, Z.; Chu, W.; Song, L.; Zhang, Z.; Yu, D.; Tian, Y.; Xie, S.; Sun, L. Large-Scale Synthesis of Nitrogen-Rich Carbon Nitride Microfibers by Using Graphitic Carbon Nitride as Precursor. *Adv. Mater.* **2008**, *20*, 1777−1781.

(31) Lee, J. M.; Lim, J.; Lee, N.; Park, H. I.; Lee, K. E.; Jeon, T.; Nam, S. A.; Kim, J.; Shin, J.; Kim, S. O. Synergistic Concurrent Enhancement of Charge Generation, Dissociation, and Transport in Organic Solar Cells with Plasmonic Metal−Carbon Nanotube Hybrids. *Adv. Mater.* **2015**, *27*, 1519−1525.

(32) Akaike, K.; Aoyama, K.; Dekubo, S.; Onishi, A.; Kanai, K. Characterizing Electronic Structure Near the Energy Gap of Graphitic Carbon Nitride Based on Rational Interpretation of Chemical Analysis. *Chem. Mater.* **2018**, *30*, 2341−2352.

(33) Tan, Y.; Zhang, Z.; Lei, Z.; Yu, L.; Wu, W.; Wang, Z.; Cheng, N. Electronic Modulation Optimizes OH* Intermediate Adsorption on Co−N$_x$−C Sites via Coupling CoNi Alloy in Hollow Carbon Nanopolyhedron Toward Efficient Reversible Oxygen Electrocatalysis. *Appl. Catal., B* **2022**, *304*, No. 121006.

(34) Zheng, Y.; Jiao, Y.; Zhu, Y.; Li, L. H.; Han, Y.; Chen, Y.; Du, A.; Jaroniec, M.; Qiao, S. Z. Hydrogen Evolution by A Metal-Free Electrocatalyst. *Nat. Commun.* **2014**, *5*, 3783.

(35) Pan, B.; Zhu, X.; Wu, Y.; Liu, T.; Bi, X.; Feng, K.; Han, N.; Zhong, J.; Lu, J.; Li, Y. Toward Highly Selective Electrochemical CO$_2$ Reduction Using Metal-Free Heteroatom-Doped Carbon. *Adv. Sci.* **2020**, *7*, 2001002.

(36) Zhou, J.; Zhang, L.; Hu, Z.; Kuo, C.; Liu, H.; Lin, X.; Wang, Y.; Pi, T.-W.; Wang, J.; Zhang, S. The Significant Role of Covalency in Determining the Ground State of Cobalt Phthalocyanines Molecule. *AIP Adv.* **2016**, *6*, No. 035306.

(37) Sorokin, A.; Kudrik, E. Phthalocyanine Metal Complexes: Versatile Catalysts for Selective Oxidation and Bleaching. *Catal. Today* **2011**, *159*, 37−46.

(38) Hu, W.; Wang, D.; Ma, Q.; Reinhart, B. J.; Zhang, X.; Huang, J. The Impact of Axial Ligation on the Excited State Dynamics of Cobalt (II) Phthalocyanine. *J. Photochem. Photobiol.* **2022**, No. 100132.

(39) Liu, Y.; Deb, A.; Leung, K. Y.; Nie, W.; Dean, W. S.; Penner-Hahn, J. E.; McCrory, C. C. Determining the Coordination Environment and Electronic Structure of Polymer-Encapsulated Cobalt Phthalocyanine Under Electrocatalytic CO$_2$ Reduction Conditions Using In Situ X-Ray Absorption Spectroscopy. *Dalton Trans.* **2020**, *49*, 16329−16339.

(40) Ha, Y.; Fei, B.; Yan, X.; Xu, H.; Chen, Z.; Shi, L.; Fu, M.; Xu, W.; Wu, R. Atomically Dispersed Co-Pyridinic N-C for Superior Oxygen Reduction Reaction. *Adv. Energy Mater.* **2020**, *10*, 2002592.

(41) Liu, W.; Zhang, L.; Yan, W.; Liu, X.; Yang, X.; Miao, S.; Wang, W.; Wang, A.; Zhang, T. Single-Atom Dispersed Co−N−C Catalyst: Structure Identification and Performance for Hydrogenative Coupling of Nitroarenes. *Chem. Sci.* **2016**, *7*, 5758−5764.

(42) Mehmood, A.; Gong, M.; Jaouen, F.; Roy, A.; Zitolo, A.; Khan, A.; Sougrati, M.-T.; Primbs, M.; Bonastre, A. M.; Fongalland, D.; Drazic, G.; Strasser, P.; Kucernak, A. High Loading of Single Atomic Iron Sites in Fe−NC Oxygen Reduction Catalysts for Proton Exchange Membrane Fuel Cells. *Nat. Catal.* **2022**, *5*, 311−323.

(43) Xiao, M.; Zhu, J.; Ma, L.; Jin, Z.; Ge, J.; Deng, X.; Hou, Y.; He, Q.; Li, J.; Jia, Q.; Mukerjee, S.; Yang, R.; Jiang, Z.; Su, D.; Liu, C.; Xing, W. Microporous Framework Induced Synthesis of Single-Atom Dispersed Fe-NC Acidic ORR Catalyst and Its In Situ Reduced Fe-N$_4$ Active Site Identification Revealed by X-Ray Absorption Spectroscopy. *ACS Catal.* **2018**, *8*, 2824−2832.

(44) Wang, J.; Huang, Z.; Liu, W.; Chang, C.; Tang, H.; Li, Z.; Chen, W.; Jia, C.; Yao, T.; Wei, S.; Wu, Y.; Li, Y. Design of N-Coordinated Dual-Metal Sites: A Stable and Active Pt-Free Catalyst for Acidic Oxygen Reduction Reaction. *J. Am. Chem. Soc.* **2017**, *139*, 17281−17284.

(45) Tian, S.; Wang, B.; Gong, W.; He, Z.; Xu, Q.; Chen, W.; Zhang, Q.; Zhu, Y.; Yang, J.; Fu, Q.; Chen, C.; Bu, Y.; Gu, L.; Sun, X.; Zhao, H.; Wang, D.; Li, Y. Dual-Atom Pt Heterogeneous Catalyst with Excellent Catalytic Performances for the Selective Hydrogenation and Epoxidation. *Nat. Commun.* **2021**, *12*, 3181.

(46) Funke, H.; Scheinost, A.; Chukalina, M. Wavelet Analysis of Extended X-Ray Absorption Fine Structure Data. *Phys. Rev. B* **2005**, *71*, No. 094110.

(47) Song, D.; Li, J.; Cai, Q. In Situ Diffuse Reflectance FTIR Study of CO Adsorbed on a Cobalt Catalyst Supported by Silica with Different Pore Sizes. *J. Phys. Chem. C* **2007**, *111*, 18970−18979.

(48) Charrad, R.; Solt, H. E.; Domján, A.; Ayari, F.; Mhamdi, M.; Valyon, J.; Lónyi, F. Selective Catalytic Reduction of NO by Methane over Co, H-SSZ-13 Catalysts: Types and Catalytic Functions of Active Co Sites. *J. Catal.* **2020**, *385*, 87−102.

(49) Bai, L.; Hsu, C.-S.; Alexander, D. T.; Chen, H. M.; Hu, X. A Cobalt−Iron Double-Atom Catalyst for the Oxygen Evolution Reaction. *J. Am. Chem. Soc.* **2019**, *141*, 14190−14199.

(50) Yin, J.; Jin, J.; Lu, M.; Huang, B.; Zhang, H.; Peng, Y.; Xi, P.; Yan, C.-H. Iridium Single Atoms Coupling with Oxygen Vacancies Boosts Oxygen Evolution Reaction in Acid Media. *J. Am. Chem. Soc.* **2020**, *142*, 18378−18386.

(51) Su, H.; Zhou, W.; Zhou, W.; Li, Y.; Zheng, L.; Zhang, H.; Liu, M.; Zhang, X.; Sun, X.; Xu, Y.; Hu, F.; Zhang, J.; Hu, T.; Liu, Q.; Wei, S. In-Situ Spectroscopic Observation of Dynamic-Coupling Oxygen on Atomically Dispersed Iridium Electrocatalyst for Acidic Water Oxidation. *Nat. Commun.* **2021**, *12*, 6118.

(52) Wei, C.; Xu, Z. J. The Comprehensive Understanding of as An Evaluation Parameter for Electrochemical Water Splitting. *Small Methods* **2018**, *2*, 1800168.

(53) Lien, H.-T.; Chang, S.-T.; Chen, P.-T.; Wong, D. P.; Chang, Y.-C.; Lu, Y.-R.; Dong, C.-L.; Wang, C.-H.; Chen, K.-H.; Chen, L.-C. Probing the Active Site in Single-Atom Oxygen Reduction Catalysts via Operando X-Ray and Electrochemical Spectroscopy. *Nat. Commun.* **2020**, *11*, 4233.

(54) Bakandritsos, A.; Kadam, R. G.; Kumar, P.; Zoppellaro, G.; Medved', M.; Tuček, J.; Montini, T.; Tomanec, O.; Andrýsková, P.; Drahoš, B.; Varma, R. S.; Otyepka, M.; Gawande, M. B.; Fornasiero, P.; Zbořil, R. Mixed-Valence Single-Atom Catalyst Derived from Functionalized Graphene. *Adv. Mater.* **2019**, *31*, 1900323.

K

(55) Jin, Z.; Li, P.; Meng, Y.; Fang, Z.; Xiao, D.; Yu, G. Understanding the Inter-site Distance Effect in Single-Atom Catalysts for Oxygen Electroreduction. *Nat. Catal.* **2021**, *4*, 615−622.

(56) Wang, Y.; Xu, A.; Wang, Z.; Huang, L.; Li, J.; Li, F.; Wicks, J.; Luo, M.; Nam, D.-H.; Tan, C.-S.; Ding, Y.; Wu, J.; Lum, Y.; Dinh, C. T.; Sinton, D.; Zheng, G.; Sargent, E. H. Enhanced Nitrate-to-Ammonia Activity on Copper−Nickel Alloys via Tuning of Intermediate Adsorption. *J. Am. Chem. Soc.* **2020**, *142*, 5702−5708.